

Photodissociation dynamics of OCS at 248 nm: The S(1D_2) atomic angular momentum polarization

M. Brouard,^{a)} A. V. Green, F. Quadrini, and C. Vallance*The Physical and Theoretical Chemistry Laboratory, The Department of Chemistry, University of Oxford, South Parks Road, Oxford OX1 3QZ, United Kingdom*

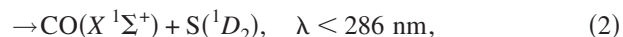
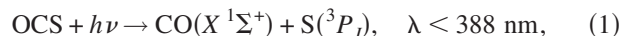
(Received 16 May 2007; accepted 19 June 2007; published online 23 August 2007)

The dissociation of OCS has been investigated subsequent to excitation at 248 nm. Speed distributions, speed dependent translational anisotropy parameters, angular momentum alignment, and orientation are reported for the channel leading to S(1D_2). In agreement with previous experiments, two product speed regimes have been identified, correlating with differing degrees of rotational excitation in the CO coproducts. The velocity dependence of the translational anisotropy is also shown to be in agreement with previous work. However, contrary to previous interpretations, the speed dependence is shown to primarily reflect the effects of nonaxial recoil and to be consistent with predominant excitation to the $2\ ^1A'$ electronic state. It is proposed that the associated electronic transition moment is polarized in the molecular plane, at an angle greater than $\sim 60^\circ$ to the initial linear OCS axis. The atomic angular momentum polarization data are interpreted in terms of a simple long-range interaction model to help identify likely surfaces populated during dissociation. Although the model neglects coherence between surfaces, the polarization data are shown to be consistent with the proposed dissociation mechanisms for the two product speed regimes. Large values for the low and high rank in-plane orientation parameters are reported. These are believed to be the first example of a polyatomic system where these effects are found to be of the same order of magnitude as the angular momentum alignment. © 2007 American Institute of Physics.

[DOI: 10.1063/1.2757618]

I. INTRODUCTION

Carbonyl sulfide (OCS) is an important atmospheric species. It is found in large concentrations in both the troposphere and the stratosphere and is a key precursor in the sulfur cycle for the production of SO₂ and sulfate aerosols.¹ In the UV region, photon absorption can give rise to dissociation via the following channels:^{2–4}



The present study is concerned with the dominant spin allowed channel [Eq. (2)], while the following paper⁵ deals with the minor, spin forbidden process [Eq. (1)], which jointly make up a unit quantum yield at 248 nm, the dissociation wavelength of the present study.²

The first UV absorption band in OCS, which peaks at 223.7 nm and extends from around 250 to 190 nm,⁶ is associated principally with a weak $2\ ^1A'(1\ ^1\Delta) \leftarrow 1\ ^1A'(X\ ^1\Sigma^+)$ transition. The transition is formally forbidden at linearity, where three states, $1\ ^1\Sigma^+$, $1\ ^1\Pi$, and $1\ ^1\Delta$, converge to the S(1D_2) product asymptote. Upon bending, the $1\ ^1\Sigma^+$ state transforms into the $1\ ^1A'$ state, while the $1\ ^1\Delta$ and $1\ ^1\Pi$ split into A' and A'' Renner-Teller pairs, ($2\ ^1A' + 1\ ^1A''$) and

($3\ ^1A' + 2\ ^1A''$), respectively, and the $2\ ^1A'(1\ ^1\Delta) \leftarrow 1\ ^1A'(X\ ^1\Sigma^+)$ transition becomes allowed through vibronic coupling.^{6–9} *Ab initio* two dimensional (2D) potential energy surfaces (PESs) for these singlet states have been reported by Suzuki *et al.*,⁴ and cuts through these PESs are shown schematically in Fig. 1. The shape of the $2\ ^1A'(1\ ^1\Delta)$ state points to an avoided crossing with a higher lying state of $^1\Delta$ symmetry. A conical intersection has been identified⁴ between the ground $1\ ^1A'(X\ ^1\Sigma^+)$ and first excited $2\ ^1A'(1\ ^1\Delta)$ states at bending angles $\sim 60^\circ$ (see Fig. 1). Suzuki *et al.*⁴ have used their calculated potentials to simulate the absorption spectrum of OCS in the first absorption band. These suggest that excitation to the $2\ ^1A'(1\ ^1\Delta)$ state contributes around 90% to the first absorption band, with the remaining 10% provided by a transition to the $1\ ^1A''$ state.^{4,7}

Early information on the photodissociation dynamics of OCS in the first absorption band was provided by studies of the nascent CO($X\ ^1\Sigma$) rotational distribution. Sivakumar *et al.* were the first to identify a bimodal rotational distribution of CO photofragments following irradiation at 222 nm.¹⁰ Furthermore, no vibrationally excited CO was found, reflecting the similarity in bond lengths of the CO group in OCS and in the free products. Sivakumar *et al.* also reported values for the spatial anisotropy parameter β for a range of CO rotational quantum states¹¹ at 222 nm. Near limiting, positive values were measured for rotational states within the minor high- J_{CO} envelope, while near-zero β values were reported for states within the major low- J_{CO} feature. It was proposed that simultaneous excitation to surfaces

^{a)}Electronic mail: mark.brouard@chem.ox.ac.uk

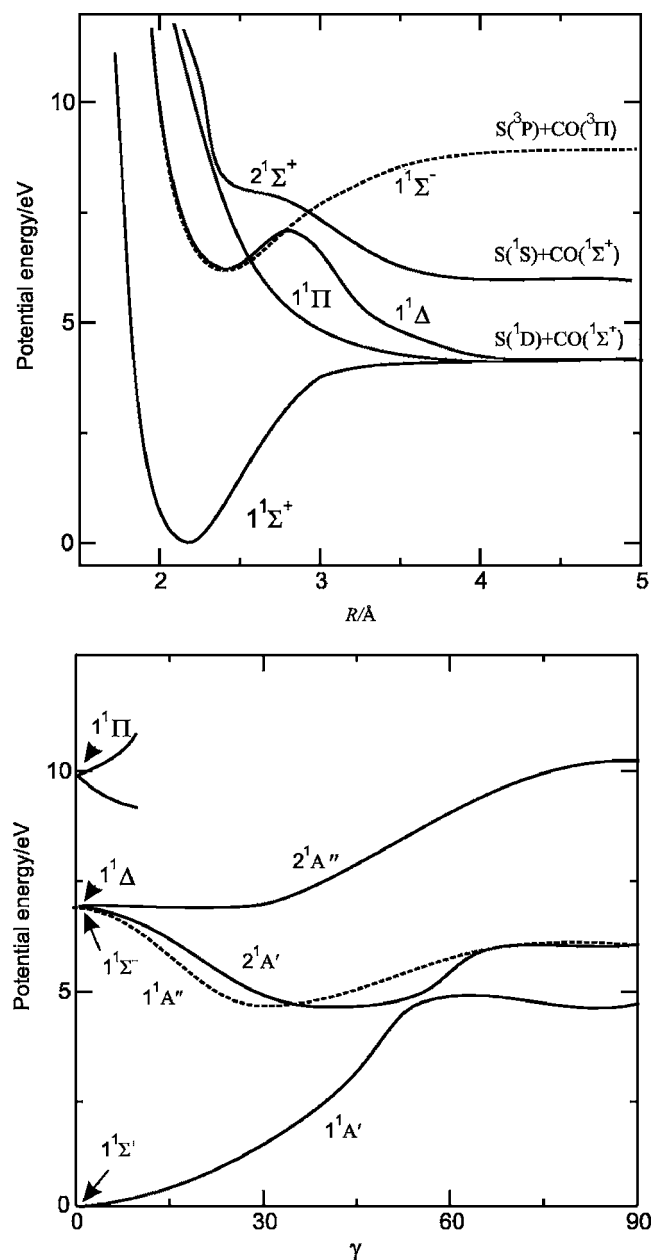


FIG. 1. Schematic representation of the singlet potential energy surfaces for OCS, adapted from those of Ref. 4, plotted as a function of (upper panel) Jacobi coordinate R , with Jacobi angle $\gamma=0^\circ$ and the C–O bond length fixed at its equilibrium value of 1.13 Å, and (lower panel) Jacobi angle γ , with the CO and CS bond lengths fixed at their equilibrium values.

of both A' and A'' symmetries was required, followed by dissociation into two different rotational distributions, possessing distinct spatial anisotropies. These measurements were subsequently extended to other wavelengths by Sato *et al.*,¹² who used the ion-imaging technique to determine CO rotational state populations and J_{CO} state dependent β parameters following excitations at 230 and 217 nm. The relative proportion of high- J_{CO} fragments was found to be enhanced at 217 nm, which was taken to imply that the A'' state, if accessed, lies lower in energy than the A' state.

In 2000 Sugita *et al.*¹³ used high resolution ion-imaging techniques to identify two rings in their images of the nascent CO photofragments following dissociation at 230 nm. The β parameters measured for a series of J_{CO} states were

found to differ for products arising from dissociation of ground state OCS(000) and bend excited OCS(010) molecules. This effect was ascribed to the interaction of the $1^1A'$, $1^1A''$, and $2^1A'$ states at bending angles, $\theta \sim 60^\circ$. Similar results were obtained by Katayanagi and Suzuki¹⁴ in one-color ion-imaging experiments in the region of the $B \leftarrow X$ transition of CO (~ 230 nm). Values of β for the ground state and hot band dissociation were used to estimate the relative contribution of excitation into the $2^1A'$ or $1^1A''$ states for each channel. On the basis of these measurements it was proposed that excitation into the $2^1A'$ state was enhanced for dissociation from vibrationally excited CO(010). The cross section for OCS(010) photoabsorption was also calculated to be at least seven times that of the OCS(000) ground state molecule.¹⁴

Recently, in a series of elegant ion-imaging studies, Janssen and co-workers made use of hexapole focusing to state select parent OCS molecules in states with specific $(v_2|JIM)$,^{15–18} where l is the vibrational angular momentum quantum number. OCS molecules were selectively studied either in their ground state or with one quantum of bending vibration, allowing independent determination of CO rotational distributions and β parameters arising in each case. At 230 nm, the speed distributions were found to be similar to those observed when the parent vibrational state was not resolved, but with the excess energy from the parent bending excitation (~ 500 cm $^{-1}$) released entirely into CO rotation.¹⁵ The β parameters for $v_2=0$ were found to be consistently lower than for $v_2=1$, particularly for low CO rotational excitation. These findings were rationalized in terms of the “parallel” transition moment function, which has greater probability at larger Jacobi angles for OCS(01 1 0) than for OCS(000), indicating that a lower population of the $1^1A''$ state would be expected for excitation from $v_2=1$ compared to $v_2=0$. In later experiments, the greater resolution afforded by the implementation of slice imaging¹⁸ allowed better separation of rings arising from hot band dissociation. Janssen and co-workers have also extended the studies to include the effects of orientation of the parent OCS molecule.^{16–18} These results are discussed in more detail in Sec. III C.

The first studies of the S-atom photofragments were provided by Sivakumar *et al.*¹¹ who used Doppler-resolved laser induced fluorescence (LIF) of $S(^1D_2)$ to confirm the interpretation of their $CO(X^1\Sigma)$ rovibrational state distributions discussed above. Subsequently, Suzuki and coworkers presented a series of ion-imaging studies of the nascent $S(^1D_2)$ photofragments,^{4,19,20} the latter work, in particular, comprising an important, comprehensive theoretical and experimental investigation of the photodissociation of OCS at various wavelengths across the first absorption band. They observed a bimodal speed distribution, with β parameters for the fast (f) and slow (s) fragments, $\beta_f=0.7$ and $\beta_s=1.8$, in good agreement with those obtained from corresponding studies on the CO fragments. 2D wave packet calculations employing the *ab initio* PESs described above revealed that the most intense feature of the speed distribution, corresponding to lower $CO(X^1\Sigma^+)$ rotational excitation, could be modeled by adiabatic dissociation on the $2^1A'(^1\Delta)$ surface, with the $1^1A''(^1\Sigma^-)$ state contributing about 10%. The $CO(X^1\Sigma^+)$ ro-

tational distributions arising from dissociation on these two PESs were found to be extremely similar, consistent with the similarity of the morphologies of the two surfaces. It was also found that the low velocity feature in the S(1D_2) distribution (arising from population of high- J_{CO} states in the CO cofragment) could only be reproduced by allowing nonadiabatic coupling between the $1^1A'$ and $2^1A'$ PESs. Since only excitation to the $2^1A'$ state could lead to the rotationally excited CO products, via crossing through the conical intersection at $\sim 60^\circ$, the variation in the amount of the “slow” fragments as a function of excitation wavelength was taken to reflect variations in the relative cross sections for excitation to the $2^1A'$ ($^1\Delta$) and $1^1A''$ ($^1\Sigma^-$) states,⁴ as previously suggested by Sato *et al.*¹² However, this feature of the dynamics was not reproduced well by the 2D dynamical calculations.⁴

In addition to the above, considerable attention has also been paid to determine the electronic angular momentum polarization of the S(1D_2) photofragments.^{4,19–26} Much of this work has been the subject of recent review,²⁷ and will be discussed further in Sec. III D. In the present paper we report the first complete characterization of the S(1D_2) angular momentum polarization for this system at 248 nm. The following section briefly describes the experimental and data analysis procedures employed. The results and discussion are presented in Sec. III. In Sec. III D we argue that the translation anisotropy data can be interpreted in terms of excitation principally to the $2^1A'$ state. In Sec. III D a long-range interaction model, described in detail previously,^{27–29} is used to help interpret the polarization data, and provide some support for the view that excitation to the $1^1A''$ plays a relatively minor role.

II. METHOD

A. Experimental procedures

The experiments were carried out using a standard velocity-map³⁰ ion imaging³¹ apparatus that has been described in detail previously.^{28,29,32–36} 1% OCS was seeded in He at a backing pressure of ~ 1 bar and expanded through a pulsed nozzle (General Valve) with a 0.5 mm diameter orifice. The molecular beam was collimated by a 1 mm diameter skimmer. The rotational temperature of the skimmed molecular beam was believed from our previous work on the same apparatus to be ≤ 25 K. Further downstream, the molecular beam was passed through a 2 mm hole in the repeller plate of the velocity mapping ion optics assembly and crossed 5 cm away from the nozzle exit by two counter-propagating laser beams. The 248 nm photolysis radiation was provided by a Lambda Physik EMG103 excimer laser, while the probe radiation, operating with a typical pulse energy of around $500 \mu\text{J pulse}^{-1}$, was obtained by frequency doubling the output of a neodymium-doped yttrium aluminum garnet pumped dye laser system. The time delay between the pump and probe laser pulses was ~ 10 ns. Two lenses of 30 cm focal length were used to focus the radiation onto the molecular beam.

The S(1D_2) photofragments were probed by (2+1) resonantly enhanced multiphoton ionization (REMPI) via the

$^1F_3 \leftarrow ^1D_2$ and $^1P_1 \leftarrow ^1D_2$ (labeled in the following as the $F\uparrow$ and $P\uparrow$) transitions at 288.1 and 291.4 nm, respectively.³⁷ During image acquisition, the probe laser wavelength was scanned over the Doppler profile of the S(1D_2) transitions in order to ensure equal detection sensitivity at all product velocities. The sulfur ions were velocity mapped onto an imaging detector consisting of a pair of 75 mm chevron double microchannel plates coupled to a P47 phosphor screen (Burle). The image on the phosphor screen was captured by an intensified charge coupled device camera (Photonic Science), electronically gated to the flight time of the detected ions, and subsequently sent to a personal computer for signal processing (thresholding, event counting,³⁸ and accumulation). Images were averaged over 25 000 laser shots. Velocity calibration of the final images was achieved using images of O(3P_J) from the photodissociation of O₂.

In order to extract information on the S(1D_2) atom polarization, images were obtained for both S-atom transitions in a variety of pump-probe laser geometries. These included the more usual geometries used previously to extract alignment parameters, and labeled HH, HV, VH, and VV according to the polarization of the pump and probe lasers lying parallel (H) or perpendicular (V) to the image plane (note that the molecular beam axis is perpendicular to the image plane). Data were also collected in other configurations, including both linearly [with the electric vector of the light at $\pm 45^\circ$ to the time-of-flight (TOF) axis] and left (L)- and right (R)-circularly polarized photolysis radiation. The use of such a large number of geometries, together with two probe transitions, helped ensure that the moments of the angular momentum distribution could be obtained unambiguously. Pairs of images were collected simultaneously by using a photoelastic modulator to switch the probe laser polarization on alternate laser shots. This procedure not only reduced the errors due to drift during an experiment but also enabled the measurement of the total angular momentum orientation, $\langle A_{10} \rangle$, and alignment, $\langle A_{20} \rangle$, from ratios of the total signal intensities in the appropriate geometries.³⁹ These parameters are required in order to normalize the image intensities, as described fully elsewhere.²⁸ Circularly polarized probe laser radiation was generated using a photoelastic modulator, and in this case, geometries were switched from L to R circular polarization on alternating laser shots. Note that in switching from L to R circularly polarized probe radiation, only the sensitivity to the odd polarization moments (orientation) is changed.

Finally, images were also recorded on alternate pairs of shots with and without firing the photolysis laser. This procedure allowed the total signal and “probe-only” ion images to be accumulated concurrently, and subsequently subtracted if necessary to remove background signal arising from ions formed through processes involving only the probe laser wavelength.

B. Data analysis

The analysis of angular momentum polarization effects by fitting Fourier moments of the ion images³² has been de-

scribed in detail previously.²⁸ The experimentally acquired images can be written in the form of a Fourier series:²⁸

$$\mathcal{I}(r, \Phi) = C_0(r) + 2 \sum_{n>0} C_n(r) \cos n\Phi + C'_n(r) \sin n\Phi, \quad (4)$$

where the Fourier moments, $C_n(r)$, can be obtained from appropriate integrals over the experimental images.³² The Fourier moments are related to a set of dynamical functions, $f'_K(q, q'; v)$, which may be derived by fitting simulated Fourier moments of the images to the experimental data. The $f'_K(q, q'; v)$ terms contain the polarization information of interest for the system.⁴⁰ They are defined as^{28,39,40}

$$f'_K(q, q'; v) = \frac{f_K(q, q'; v)}{\langle f_0(0, 0; v) \rangle + 2 \langle f_0(1, 1; v) \rangle},$$

where $\langle f_K(q, q'; v) \rangle$ represent the integral of the dynamical functions over recoil speed. In the present work, the speed dependence of the dynamical parameters is expressed as a linear combination of Gaussian functions centered at a series of equally spaced speeds, v_i :

$$f'_K(q, q'; v) = N \sum_{i=0}^{i_{\max}} a_K(q, q'; i) e^{-\sigma(v_i - v)^2}, \quad (5)$$

where N is a normalization constant, $a_K(q, q'; i)$ are Gaussian specific polarization parameters, σ is a width parameter, and v_i are the Gaussian centers. In practice, the $f'_K(q, q'; v)$ dynamical functions are usually recast in terms of a variety of different (but equivalent) factors, including the polarization parameters of Rakitzis and Zare⁴¹ and the polarization anisotropy parameters of Vasyutinskii and co-workers.^{39,42-44} For comparison with previous work, both sets are used here.

The best-fit coefficients $a_K(q, q'; i)$ for a given number of Gaussians, $i_{\max}=30$, were determined using a genetic algorithm which selected from a pool of parameters randomly generated within the constraints of the physically allowed values. A Monte Carlo procedure, described fully elsewhere,³² was then used to determine the errors on the fitted coefficients and on the speed dependent moments of the angular distribution. To reduce the number of fitting coefficients, the speed dependence of the polarization parameters was reexpressed in terms of a Legendre polynomial expansion.²⁸ The fitted coefficients for all polarization parameters from Eq. (5) [excluding those for the speed distribution, characterized by the set of coefficients $a_0(i) \equiv a_0(0, 0; i) + 2a_0(1, 1; i)$] were expressed as a convolution of the speed distribution parameters and a Legendre polynomial ($P_l(\cdots)$) series with n_{Leg} , the maximum order, set to 5:

$$a_K(q, q'; i) = a_0(i) \sum_{l=0}^{n_{\text{Leg}}} b_K(q, q'; l) P_l(x_i), \quad (6)$$

where

$$x_i = 2 \frac{i - 1}{i_{\max} - 1} - 1. \quad (7)$$

This procedure allowed for the speed dependence of the polarization parameters, while significantly reducing the basis set size.

In the case of diatomic molecules, the dynamical functions have been interpreted in terms of contributions to the dynamics by transitions to the dissociation continuum with their transition dipole moment vectors lying either parallel ($q, q'=0$) or perpendicular ($q, q'=\pm 1$) to the bond axis.⁴⁵ Interpretation of the polarization parameters in the case of larger systems^{42,46} is more problematic and awaits a detailed theoretical treatment. Here, as previously,^{27-29,34} we have used the polarization parameters to determine the molecular frame state multipoles, $\rho_{KQ}^{\text{mol}}(\theta; v)$, using the equations given elsewhere.^{28,39} These molecular frame parameters are functions of velocity and angle θ between the recoil direction and the electric vector of the photolysis light.

III. RESULTS AND DISCUSSION

A. Ion images

Images were collected using two REMPI transitions, with eight pump-probe polarization geometries, yielding a total of 16 experimental images. A selection of the summed, processed images obtained using the REMPI transition via the 1P_1 intermediate state is shown in Figs. 2 and 3. Alongside the images are shown their Fourier moments, $C_n(r)$, and fit to them using a single simultaneous global fit to all the data. The transition used for the images shown has a large line strength factor for polarization parameters of rank $K=4$. Of particular interest are the HH and VH geometries (shown in Fig. 2), for which large C_6 and C_4 moments are measured. These are the fingerprint of high-order alignment, indicating that in the present system, $K=4$ parameters play an important role. The geometries used to obtain the results shown in Fig. 3 are sensitive to orientation as well as alignment effects. Due to the line strength factors, images recorded using the 1P_1 intermediate state are sensitive to $K=1$ orientation, while the 1P_1 intermediate allows the independent probing of $K=3$ parameters. Differences between images recorded using alternating left- and right-circularly polarized light reveal that all orientation parameters are non-zero for the present system.

B. Speed distribution

The speed distribution recovered from fits to the data is shown in the top panel of Fig. 4. The middle panel of the same figure shows the same distribution plotted as a function of the fraction of the available energy released into CO cofragment rotation (f_{rot}), where it is compared with distributions from the work of Suzuki *et al.*⁴ and van den Brom *et al.*¹⁵ Excellent agreement is found between the data collected by Suzuki *et al.* at 248 nm (Ref. 4) and the present study. The data by van den Brom *et al.*¹⁵ are that arising from photodissociation of ground state OCS(000) and vibrationally excited OCS(01¹0). Given that these distributions are quite similar it seems reasonable to interpret the present data in terms of dissociation of ground state OCS(000) molecules, while bearing in mind that dissociation of vibrationally excited OCS is likely to play some role under the present experimental conditions, particularly at high fragment speeds. If OCS bending excitation is neglected, the corresponding CO($X^1\Sigma^+$) rotational distribution can be cal-

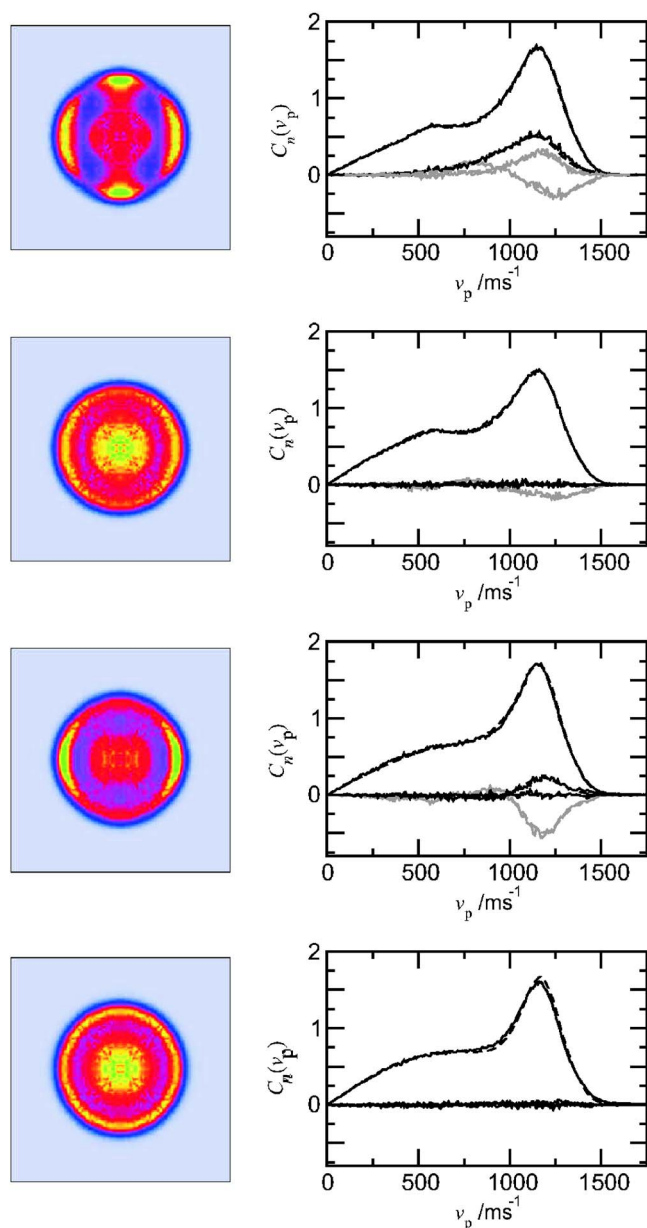


FIG. 2. (Color online) Images, Fourier moments (—), and fits (---) for $S(^1D_2)$ products probed via the 1P_1 intermediate. Pump-probe geometries, from top to bottom: HH, HV, VH, and VV. Nonzero experimental and fitted C_2 and C_6 moments are shown in gray. In the top panel, the C_6 term is positive.

culated to peak at $J_{CO}=26$, with a secondary maximum at $J_{CO}=49$. These values are shifted to $J_{CO}=30$ and $J_{CO}=51$ if excitation is assumed to occur exclusively from OCS(010).

In Table I we compare the relative populations of fast and slow fragments from this study with those obtained previously at 288 nm,²⁴ 230 nm,²¹ 230 nm,⁴ and 193 nm.²⁶ A steady increase is seen in the population of the slow channel with increasing excitation energy, starting from no contribution at 288 nm, and reaching up to a 50% weight at 193 nm. As noted in Sec. I, this trend has been reported previously,^{4,12} where it was ascribed to the balance of optical excitation to the $2^1A'$ and $1^1A''$ states. Recall that only population of the $2^1A'$ state is thought to lead to the generation of slow, rotationally excited fragments via nonadiabatic crossing to the

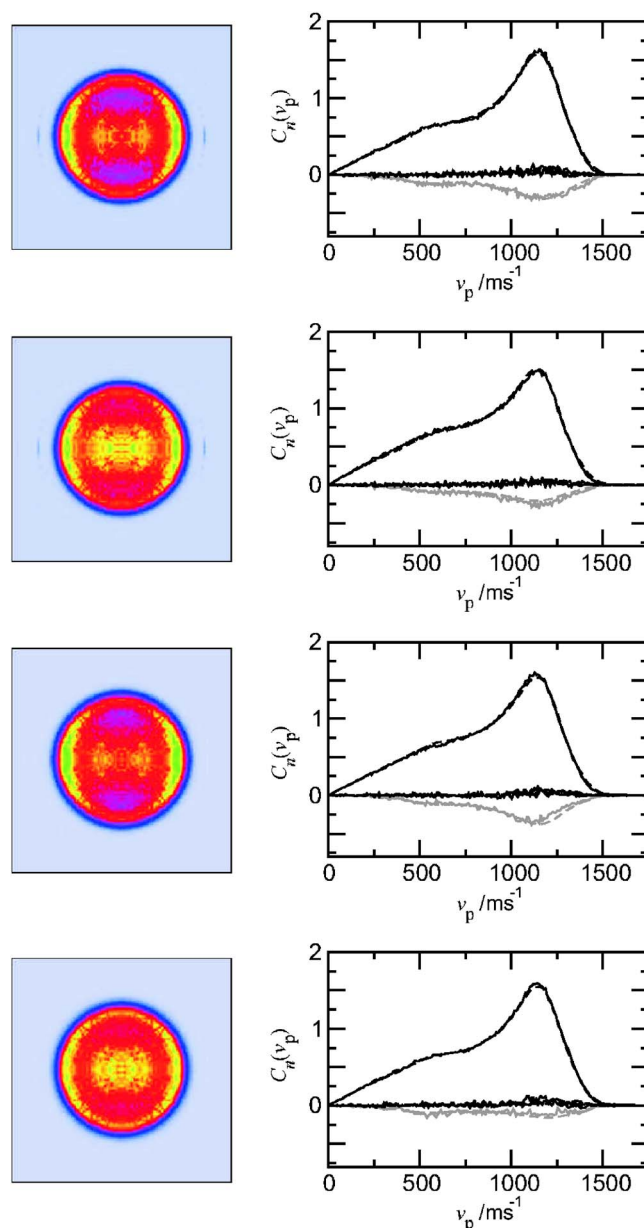


FIG. 3. (Color online) Images, Fourier moments (—), and fits (---) for $S(^1D_2)$ products probed via the 1P_1 intermediate. Pump-probe geometries, from top to bottom: $-45L$, $-45R$, RL , and RR . Nonzero experimental and fitted C_2 moments are shown in gray.

ground $1^1A'$ state. However, as noted by Lee *et al.*,²⁶ the increasing intensity of the slow peak with decreasing wavelength might also reflect the increase in the nonadiabatic crossing probability with increasing relative speed of the fragments. This explanation is perhaps more likely in the light of the discussion of $\beta(v)$ to follow in Sec. III C

Inspection of Fig. 4 reveals that the main peak of the internal energy distribution shifts to higher f_{rot} with decreasing wavelength, indicating that a greater proportion of excess energy is released into rotation. By contrast, the position of the secondary minimum remains largely unaffected by wavelength, peaking at $f_{rot} \sim 0.8$ – 0.9 . The trends in f_{rot} for the two peaks imply different origins for CO fragment rotation in the two speed regimes. The roughly constant f_{rot} for the slow fragment suggests that these products access a specific,

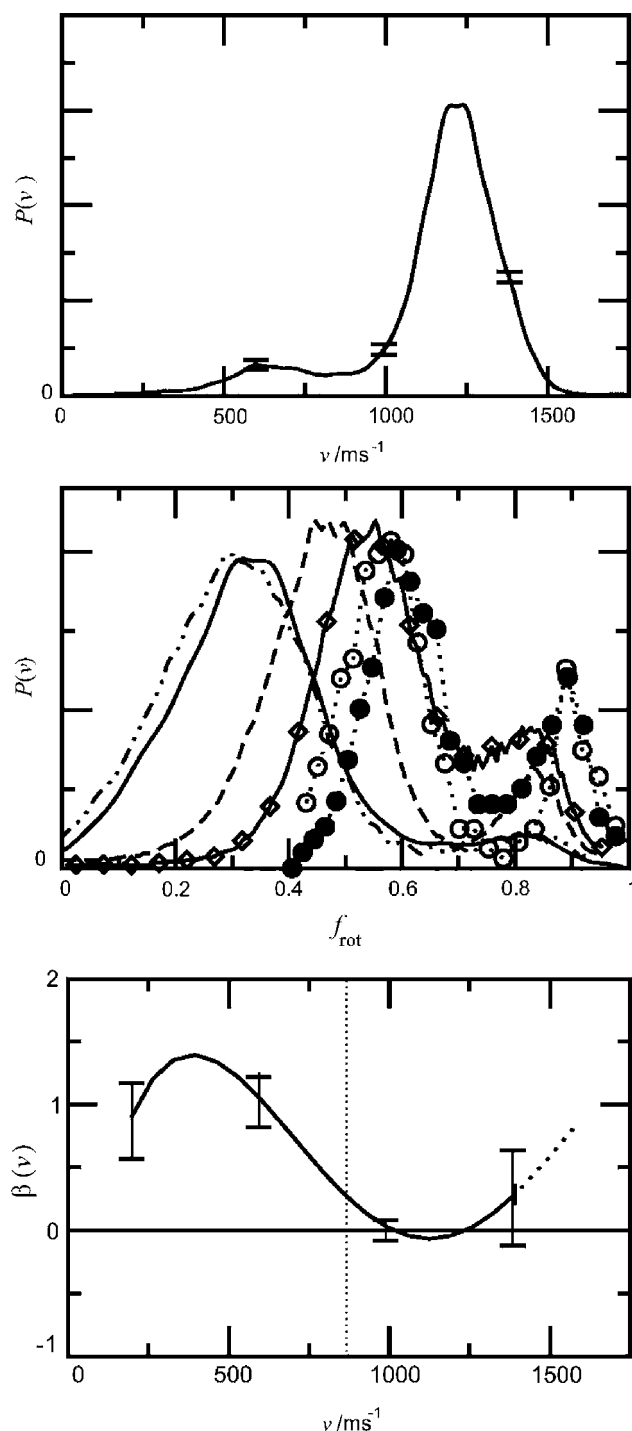


FIG. 4. Upper panel: The speed distribution for the $S(^1D_2)$ product returned from fits to the experimental data; some of which is shown in Figs. 2 and 3. Error bars indicate 1σ confidence limit. Middle panel: Speed distribution plotted as a function of the fractional rotational energy release. The current work (—) is compared with data by Suzuki *et al.* (Ref. 4) at 248 nm (— — —), 235 nm (— · — · —), and 223 nm (— ◊ —) and data by Van den Brom *et al.* (Ref. 15) for OCS(000) (○) and OCS(01¹0) (●) following dissociation at 230 nm. Bottom panel: As in the top panel, but showing speed dependence of the translational anisotropy parameter. The region drawn with a dotted corresponds to fragments that are produced from photodissociation of internally excited OCS. The minimum in the speed distribution between “slow” and “fast” peaks is indicated by a faint vertical dotted line.

highly bent geometry independent of photon energy. This probably reflects the geometry in the region of the conical intersection between the $2^1A'$ and $1^1A'$ states which trajectories must funnel through in order to dissociate on the

TABLE I. Relative populations and average spatial anisotropy parameters for fast and slow fragments at a range of wavelengths within the first absorption band. Note that Kim *et al.* reported a value of $\beta_f=0.20$ following dissociation at 223 nm (Ref. 21). The values at 223 nm are also similar to the average of those determined by Sivakumar *et al.* using Doppler-resolved LIF of the CO photofragments (Ref. 11).

	288 nm ^a	248 nm	230 nm ^b	223 nm ^c	193 nm ^d
N_s	0	0.18	0.21	0.25	0.49
N_f	1	0.82	0.79	0.75	0.51
β_s	...	0.73	1.6	1.8	0.8
β_f	−0.70	−0.02	0.3	0.7	0.4

^aReference 24.

^bReference 15.

^cReference 4.

^dReference 26.

ground state. It would seem that the main torque on the CO group is generated on the way to the conical intersection, with only modest torques experienced by the system after the crossing region.

The variation of f_{rot} with wavelength observed for the fast fragments can be attributed to at least two factors. As the available energy is altered, different regions of the PES for the $2^1A'$ state become accessible, potentially leading to different degrees of rotational energy release into the products. Suzuki *et al.*⁴ employed 2D quantum dynamical calculations to determine the CO rotational distributions arising from photodissociation on the $2^1A'$, $1^1A'$, and $1^1A''$ surfaces. These calculations were not quantitatively accurate, and the authors had to correct the calculated rotational energies by 3700 cm^{-1} in order to reconcile theory and experiment at 223 nm. However, with this correction, the rotational energy release distributions arising from dissociation on the coupled $2^1A'$ and $1^1A'$ surfaces were found to have a main peak at $f_{\text{rot}}=0.60$ at 223 nm, 0.51 at 235 nm, and 0.27 at 248 nm. The latter estimate compares very favorably with the distribution observed here, which peaks at around $f_{\text{rot}}=0.3$ (see Fig. 4).

Another possible explanation for the variation in rotational excitation with photolysis wavelength is that it reflects the varying ratio of excitation to the $1^1A''$ and $2^1A'$ PESs and possible differences in the subsequent dissociation dynamics on these surfaces. However, in the light of the discussion in the next section, and the fact that the calculations of Suzuki *et al.*⁴ indicated a relatively minor ($\sim 10\%$) role for excitation into the $1^1A''$ state, independent of wavelength between 248 and 223 nm, this explanation seems less likely. Furthermore, note that the $1^1A''$ state is predicted to yield a hotter rotational distribution than the $2^1A'$ state,⁴ the opposite to that required to account for the trends shown in Fig. 4.

C. β parameter

The $\beta(v)$ parameter recovered from the fits to the data is shown in the bottom panel of Fig. 4. The data are replotted as a function of the rotational quantum state of the cofragment in Fig. 5, where the results are compared with previous work obtained at other dissociation wavelengths. The trend in $\beta(v)$ with velocity observed here closely follows that measured

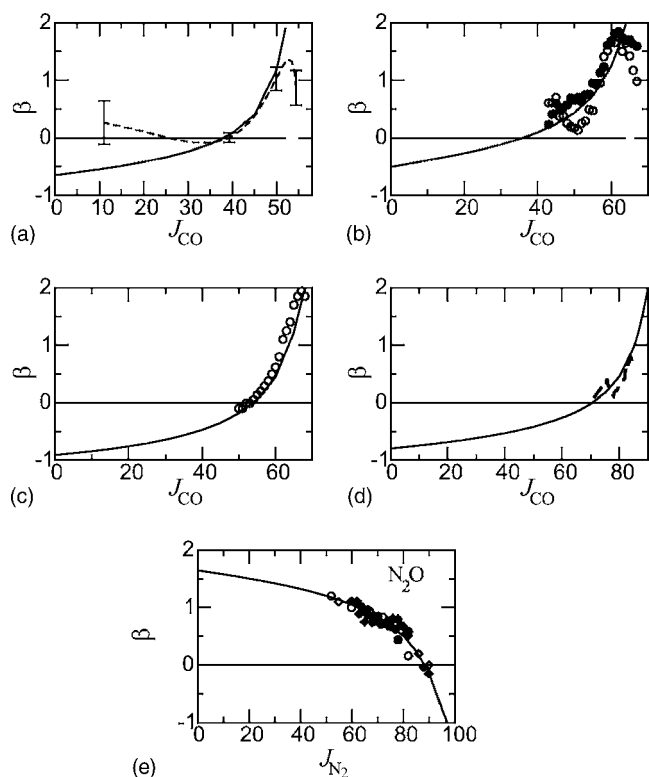


FIG. 5. Predictions of the model (shown as the continuous solid line in each figure) of the dependence of β on the rotational state of the molecular cofragment (Ref. 47). The predictions are compared with data for (a) the photodissociation of OCS at 248 nm from the present work, (b) the selective photodissociation of OCS in $v_2=0$ (\circ) and $v_2=1$ (\bullet) at 230 nm from Ref. 15, (c) the photodissociation of OCS at 222 nm from Ref. 11, (d) the photodissociation of OCS at 193 nm from Ref. 26, and (e) the photodissociation of N₂O at 203–205 nm from Refs. 51–54. The model parameters were (a) $R_f=2.9$ Å, $\delta=72^\circ$; (b) $R_f=2.5$ Å, $\delta=65^\circ$; (c) $R_f=2.0$ Å, $\delta=80^\circ$; (d) $R_f=2.5$ Å, $\delta=75^\circ$; and (e) $R_f=2.8$ Å, $\delta=-20^\circ$.

before.^{4,11,15,26} The speed averaged values of β , resolved into slow and fast components, are compared with previous results in Table I.

As noted in Sec. I, values of β_f for the fast fragments have previously been attributed to excitation into a mixture of the $2^1A'$ and $1^1A''$ states. Under this assumption, β_f can be used to make a crude estimate of the proportion of $A'(f_{A'})$ and $A''(f_{A''})$ participation in the fast channel:

$$\beta_f = f_{A'}\beta_{\parallel} + (1 - f_{A'})\beta_{\perp},$$

where β_{\parallel} and β_{\perp} are anisotropy parameters contributing to β_f from parallel and perpendicular transitions. Setting $\beta_{\perp}=-1$ and $\beta_{\parallel}=+2$, the limiting values in the case of diatomic molecular photodissociation under the axial recoil approximation lead to $f_{A'} \sim 0.33$ at 248 nm. This value fits in with the general trend of values estimated from the previous work over a range of wavelengths.^{4,21,22,24,26} Given the proposed energy ordering of the two initially excited electronic states ($1^1A'' < 2^1A'$),⁴ which would favor accessing the $1^1A''$ state at longer wavelengths, an overall reduction in β might be expected as the dissociation wavelength is increased, broadly in agreement with experimental observation.

A more quantitative explanation for the variation of $\beta(v)$ with fragment speed and wavelength must allow for the

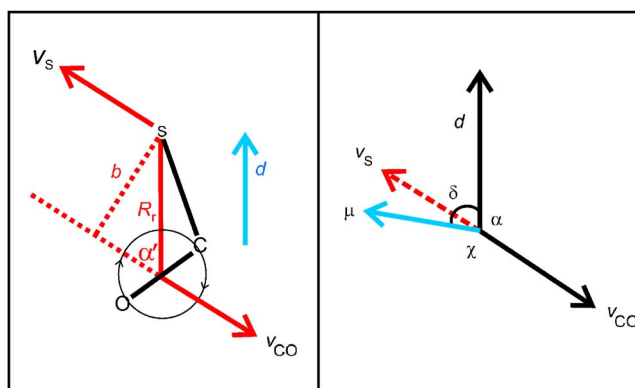


FIG. 6. (Color online) Parameters used to model the speed dependence of the translational anisotropy parameter shown in Fig. 5 (Ref. 47). Left panel: The definition of the exit impact parameter b , and the Jacobi length R_f at which CO rotation is established. d represents the direction of R at the instant of excitation. This axis is assumed to lie nearly parallel to the permanent dipole moment in the ground state OCS molecule (Ref. 17). Right panel: Following van den Brom *et al.* (Ref. 17), the definition of the angles α , χ , and δ . Note that $\alpha' = 180 - \alpha$ and $\chi' = 180 - \chi$.

breakdown of the axial recoil approximation. The effects of non-axial recoil may be significant, particularly for the slowest fragments, as discussed previously by Lee *et al.*²⁶ and Janssen and co-workers.^{17,18} We use a simple classical model, described by Demyanenko *et al.*,⁴⁷ to account for nonaxial recoil by estimating the deflection angle of the S atom arising from rotational excitation of the CO cofragments (see Fig. 6). In the absence of rotation of the parent OCS molecule, conservation of angular momentum means that the magnitude of the angular momentum of the CO product, J_{CO} , can be equated approximately to the magnitude of the total orbital angular momentum for the system, such that

$$|L| = \mu v_{\text{rel}} b = \hbar \sqrt{J_{CO}(J_{CO} + 1)},$$

where b is the exit impact parameter, and μ and v_{rel} are the reduced mass and (asymptotic) relative speed of the atom-diatom system. If we assume that fragment rotation is established at some Jacobi distance, R_f , then the impact parameter can be used to determine a deflection angle from linearity $\alpha' = \sin^{-1}(b/R_f)$. The corresponding β parameter can be written approximately^{26,47} as

$$\beta \approx 2P_2(\cos \chi'),$$

where χ' is the angle between the velocities of the S atom v_S , and μ , the transition dipole moment in OCS. We assume that the latter lies at some angle δ to the direction of R at the instant of excitation, which we label d in Fig. 6. This axis is assumed to lie nearly parallel to the permanent dipole moment in the ground state OCS molecule.¹⁷ On the assumption that the vectors shown in Fig. 6 are all coplanar, it follows that $\chi' = \delta - \alpha'$. The $\beta(v)$ parameters estimated using this model, employing R_f and δ as adjustable parameters, are shown in Fig. 5, where they are compared with the present experimental results, and previous data at 230 nm,¹⁵ 223 nm,¹¹ and 193 nm.²⁶ By assuming that the transition moment in OCS is tilted away from the initial OCS linear axis (i.e., $\delta \neq 0$) the experimental and calculated values of $\beta(v)$ at

all wavelengths shown may be reconciled *without* the need to invoke the participation of the $1^1A''$ state. The tilt of μ away from the initial axis is found to be between 65° and 80° , with the values increasing somewhat within this range towards shorter photolysis wavelengths. The values of R_r returned by the simulations are centered around 2.5 \AA , which, quite reasonably, is slightly larger than the Jacobi length, R_e , in the equilibrium ground state geometry of OCS. Note that the effect of nonaxial recoil on the “fast” fragments is only a few degrees, and the consequent change in β is modest, suggesting that the use of the axial recoil approximation for the fast products is much more reasonable than for the slow products. The foregoing discussion neglects consideration of the effects of the vibrational angular momentum of OCS, which could lead to rotation of the excited OCS molecule out of the plane defined in Fig. 6. Because only small values of l are likely to be accessed in the present experiments, we believe that the effects of nonzero values of l will be minimal in the present experiments, as discussed further in Sec. III D 2.

The theoretical calculations of Suzuki *et al.* predict that between 223 and 248 nm the $1^1A''$ state contributes a near constant fraction of about 10% to the total absorption cross section.⁴ Such a small contribution has little effect on the predictions of the model. Although it is possible that the $1^1A''$ states contribute a larger fraction to a specific subset of rotational states, the simulations do not require such an enhanced contribution to account well for the experimental data in the wavelength region of 248–193 nm. Simulations (not shown) were also carried out to model the β parameters obtained by Kim *et al.* at 288 nm,²⁴ in their one-color dc slice imaging study of the photodissociation dynamics of OCS. Although these one-color experiments did not allow alignment parameters to be determined, the speed distribution and “effective” values of $\beta(v)$ (uncorrected for the presence of angular momentum alignment) could be obtained reliably. Because the effective $\beta(v)$ parameters were found to be reasonably constant, and always negative, Kim *et al.* concluded that the $1^1A''$ transition strongly dominates the dynamics at this wavelength. In contrast to the simulations at shorter wavelengths, a fit to these results at 288 nm required a much larger, unrealistic value of $R_r \sim 5 \text{ \AA}$. Exceptionally in this case, a satisfactory simulation using $R_r \sim 2.5 \text{ \AA}$ and $\delta = 70^\circ$ could only be achieved by including a 50% contribution from the $1^1A''$ state. The latter was assumed to contribute equally to all rotational states of the products with an associated β parameter of -1 . Apart from the above data obtained at the extreme red end of the absorption band, the simulations suggest that the role of the $1^1A''$ state might be much less important than previously inferred on the basis of analysis of the nonlimiting β values. It is proposed that the latter arise primarily as a result of the effects of nonaxial recoil.

Another important feature of the S-atom speed or CO rotational state dependence of the β parameter is that, as seen from Fig. 5, there is no dramatic change in the trend in values between the fast and slow channels. The implication is that as far as β is concerned, the division into fast and slow fragments is somewhat arbitrary. Thus, while the bimodal speed distribution principally reflects the effects of adiabatic

and nonadiabatic dissociation pathways subsequent to excitation to the $2^1A'$ state, the translational anisotropy parameter is sensitive largely to the direction of the transition dipole moment associated with this excitation and to angular momentum conservation constraints.

The *ab initio* calculations of Suzuki *et al.*⁴ predict that in the Franck-Condon region (which lies close to, but not exactly at, linearity), the transition dipole moment lies quite close to the C—S bond axis. This result is at variance with the conclusions based on the simulations, which find that μ is aligned around 70° from the Jacobi vector R at the instant of excitation. In the calculations of Balint-Kurti and co-workers^{48,49} on the isovalent N_2O molecule, discussed further below, it was found that the transition dipole moment function was very sensitive to basis set. The orientation of the transition dipole moment for the $2^1A' \leftarrow 1^1A'$ band of OCS would certainly merit further theoretical investigation.

As noted in Sec. I, Janssen and co-workers have studied the photodissociation of oriented OCS molecules.^{16,17} These experiments allowed the angle δ between μ and the direction of the permanent dipole moment in OCS, d , to be measured directly for the photodissociation of oriented OCS(01^10) molecules at 230 nm. Janssen and co-workers obtained a tilt angle of only $\sim 31^\circ$ for CO molecules born at high J_{CO} .^{16,17,50} However, the equations used to fit the ion images allow another solution, yielding a tilt angle of 63° ,^{16,17,50} very close to the value obtained here from the simulation of the velocity dependence of $\beta(v)$. Furthermore, similar values of δ can be obtained over the full range of J_{CO} states investigated by Janssen and co-workers,^{16,17} again without the need to invoke significant participation by the $1^1A''$ state. The diagram on the right side of Fig. 6 illustrates the proposed mutual orientation of the relevant vectors. More recently, in similar state-to-state experiments at $\lambda \sim 230 \text{ nm}$, Lipciuc and Janssen have measured β for dissociation into high rotational states of CO.¹⁸ They found that for OCS initially in $v_2=0$, the β parameter for $J_{CO}=63$ changed significantly from 1.52 to -0.33 with a decrease in available energy of as little as 1000 cm^{-1} .¹⁸ Interestingly, under the conditions described, the model suggests that with $\delta=65^\circ$ and $R_r=2.5 \text{ \AA}$ a reduction of 1000 cm^{-1} causes this fragment channel to become closed by angular momentum conservation. Thus, with the reduction in available energy, these high rotational states of CO are produced from trajectories experiencing unusually high torques, which in the model require large R_r . This might reflect a minor dissociation pathway on a different surface, perhaps the $1^1A''$ surface, which would certainly be consistent with the change in sign of β .

To provide support for the model simulations described above for OCS we have also undertaken simulations of the velocity dependent $\beta(v)$ parameters generated upon photodissociation of the isovalent N_2O molecule. The results of these simulations are shown in panel (e) of Fig. 5. Excellent agreement between experiment^{51–54} and the model can be obtained once more, this time employing the tilt angle $\delta=-20^\circ$ and $R_r=2.8 \text{ \AA}$. As with OCS, this agreement is achieved without the need to invoke the participation of the analogous $1^1A''$ state. In the case of N_2O , the seemingly

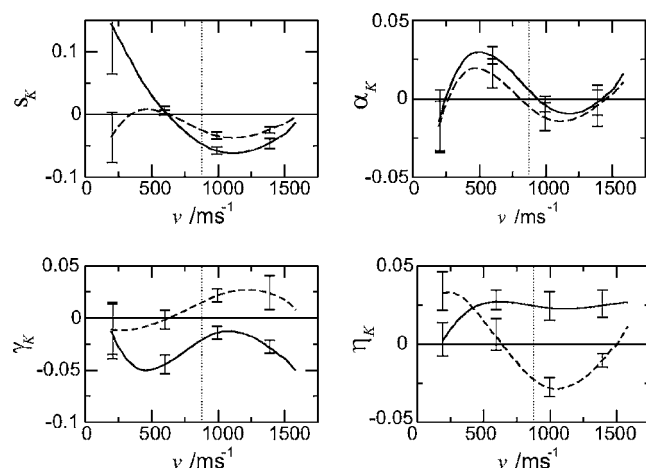


FIG. 7. Speed dependent angular momentum alignment parameters returned from fits to the data for the S(1D_2) product. $K=2$ (—), $K=4$ (---). The minimum in the speed distribution between “slow” and “fast” peaks is indicated by a vertical dotted line. Error bars indicate 1σ confidence limit.

minor role played by the $1^1A''$ state, together with the preferential alignment of μ along the N—O bond, is in reasonable accord with recent *ab initio* calculations of Balint-Kurti and co-workers^{48,49} and Nanbu and Johnson.⁵⁵ Interestingly, the parameter $R_r=2.8$ Å, which provides some measure of the torque generated on the excited state surface, is very similar to the values obtained above for OCS. This is reassuring because the bending potentials calculated for the two systems are quite similar,^{4,48,49,55} so similar torques would be expected to operate during dissociation. Further comparisons between N₂O and OCS are made in Sec. III F.

D. Orbital alignment

The speed dependent alignment and orientation parameters are shown in Figs. 7 and 8, respectively, with the speed averaged values given in Table II. Note that the speed dependence of many of these parameters follows quite closely the speed dependence of the translational anisotropy discussed above. As with previous work on this system,^{4,25,26} because

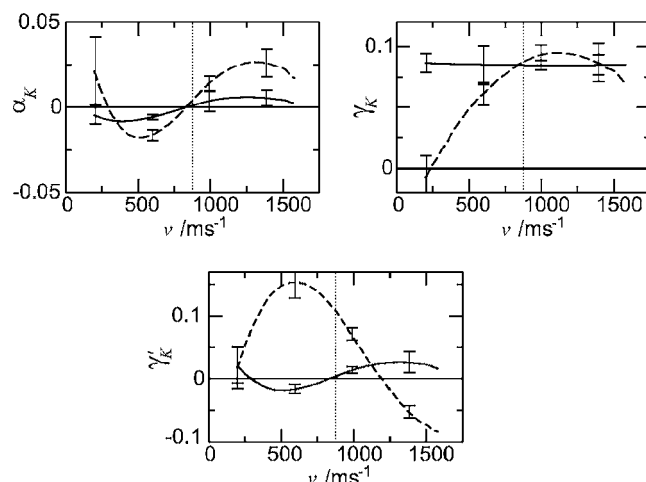


FIG. 8. Speed dependent angular momentum orientation parameters returned from fits to the data for the S(1D_2) product. $K=1$ (—), $K=3$ (---). The minimum in the speed distribution between “slow” and “fast” peaks is indicated by a vertical dotted line. Error bars indicate 1σ confidence limit.

TABLE II. Spatial anisotropy and polarization parameters for S(1D_2) fragments, speed averaged, and for the slow (peaking at ~ 600 m s⁻¹) and fast (peaking at ~ 1200 m s⁻¹) speed regimes. 1σ errors reported refer to the last digit(s) shown. A discussion of the error analysis can be found elsewhere. (Ref. 32).

	Average	Slow	Fast
$N(v)$		0.18(4)	0.82(2)
β	0.078(10)	0.73(10)	-0.02(2)
α_1	0.004(4)	-0.003(2)	0.006(5)
γ_1	0.085(4)	0.085(5)	0.085(4)
γ'_1	0.024(5)	0.012(7)	0.025(5)
s_2	-0.049(4)	0.007(4)	-0.057(5)
α_2	-0.003(2)	0.022(5)	-0.007(5)
γ_2	-0.021(4)	-0.040(9)	-0.018(4)
η_2	0.026(6)	0.025(6)	0.023(6)
α_3	0.019(3)	-0.010(3)	0.024(5)
γ_3	0.090(10)	0.072(10)	0.092(10)
γ'_3	0.011(2)	0.141(15)	-0.006(6)
s_4	-0.029(3)	-0.004(3)	-0.033(4)
α_4	-0.008(5)	0.011(9)	-0.011(7)
γ_4	0.022(4)	0.000(9)	0.026(4)
η_4	-0.019(3)	0.003(10)	-0.022(4)

the speed distribution exhibits a clear bimodality, the spatial anisotropy and polarization parameters are tabulated separately for the two speed regimes. Significant differences are observed between the angular momentum distributions for the S atoms born in the two speed regimes. This behavior is not surprising since, in addition to the nonaxial recoil effects discussed above in the context of β , the orbital angular momentum polarization also reflects in part the long-range dynamics of the system, which are thought to be different for the fast and slow fragments. In the following we will restrict attention to the polarization parameters averaged over the two speed regimes, as shown in Table II, although, in the light of the above discussion, any consideration of the polarization of the slow photofragments should allow for the effects of nonaxial recoil. In the absence of a rigorous theory of these effects in polyatomic systems, it is perhaps premature to speculate on the nature of the speed dependence of the polarization parameters (or their J_{CO} quantum-state resolved values). However, in view of the likely origins of the speed dependence of $\beta(v)$, discussed in Sec. III C, it seems reasonable to suppose that the speed dependence of the polarization parameters will follow similar trends to $\beta(v)$, as appears to be the case from the relatively low resolution data shown in Fig. 7. A more detailed study, involving the measurement of the S-atom polarization as a function of cofragment rotational state, J_{CO} , would clearly be of interest and is now feasible using very high resolution ion-imaging techniques.¹⁸

Although none of the polarization parameters approach their limiting values, all were found to be nonzero, apart from γ_4 for the slow fragments. The high rank orientation ($K=3$) and alignment ($K=4$) parameters are particularly large, in most cases being of similar magnitude to, if not

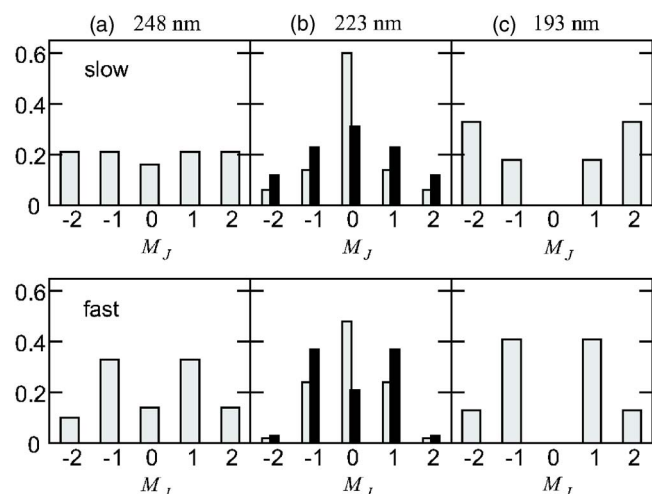


FIG. 9. Scattering angle averaged M_J populations for slow fragments (top row) and fast fragments (bottom row) following dissociation at (a) 248 nm (this work), (b) 223 nm (Ref. 4) (light gray) and (Ref. 25) (black), and (c) 193 nm (Ref. 26).

larger than, their lower rank ($K=1,2$) counterparts. The Laboratory frame polarization parameters reported in Table I have been used to construct the molecular frame angular momentum distribution, characterized by the J -state multipoles $\rho_{KQ}^{\text{mol}}(\theta)$ for the fast and slow atomic products.²⁸ [The full set of speed averaged $\rho_{KQ}^{\text{mol}}(\theta)$ moments is presented below in Sec. III D 1.] The speed averaged diagonal ($Q=0$) elements of $\rho_{KQ}^{\text{mol}}(\theta)$ provide information on the M_J populations of the slow and fast fragments. These are compared with previously reported values in Fig. 9. Both slow and fast fragments exhibit nonisotropic populations. The polarization of the slow fragments is mild and preferentially directed along \mathbf{v} , while the faster fragments have a more marked population bias towards $M_J=1$.

Rakitzis *et al.* have reported a complete characterization of the $S(^1D_2)$ atomic alignment following dissociation at 223 nm.²⁵ In this work the polarization parameters were recovered using a carefully selected set of Abel-invertible images, and our findings are in broad agreement with those of that study,²⁵ as seen from Fig. 9. Kim *et al.* have recently used dc slicing techniques to examine the photodissociation dynamics of OCS at 193 nm. Four rings were identified in the speed distribution of the $S(^1D_2)$ atoms, the slowest corresponding to probe-only dissociation, as investigated in their previous work,²⁴ one (termed ring C, peaking at $J=84$) broadly corresponding to the slow fragments, and two rings (termed A and B, peaking at $J=76,79$) which were associated with the single fast regime at longer wavelengths.²⁶ As with the present experiments, a marked preference for $M_J=1$ was observed for the fast fragments born in “ring B.” The preference for $M_J=0$ observed by Katayanagi and co-workers^{4,19} is at odds with the present results and with those of Rakitzis *et al.*,²⁵ who reported M_J populations at the same wavelength, 223 nm. It is possible that the discrepancy is due to the reduced parameter fit used by Suzuki *et al.*^{4,19,20} Unlike the present work, their analysis assumed that the distribution of the angular momentum \mathbf{J} was cylindrically symmetric about the recoil velocity \mathbf{v} and was independent of scattering angle.

TABLE III. $\mathbf{a}_0^K(p)$ for $S(^1D_2)$ fragments arising from dissociation at 248 nm (this work), 230 nm [Rakitzis *et al.* (Ref. 22)], 223 nm [orientation—Kim *et al.* (Ref. 21); alignment—Rakitzis *et al.* (Ref. 25)], and 193 nm [Lee *et al.* (Ref. 26)]. In the latter case, the slow fragments are assumed to be those associated with ring C, while for the fast fragments data for B are given, with errors estimated from the parameters shown graphically in Ref. 26. The conversions between the parameters shown in Table II and those given here were taken from Alexander (Ref. 46) for the $K=1$ and 2 moments and from Vasyutinskii (Ref. 69) for $K=4$. Note that the definitions of the $\text{Re}[\mathbf{a}_1^K(\parallel, \perp)]$ moments in the latter are a factor of 2 smaller than the definitions of Rakitzis *et al.* (Ref. 22).

	248 nm	230 nm ^a	223 nm ^b	193 nm ^c
Slow				
β	0.73(10)	1.60(10)	1.40(20)	0.80(-)
$\text{Im}[\mathbf{a}_1^1(\parallel, \perp)]$	-0.03(0)		~ 0	-0.02(1)
$\mathbf{a}_0^2(\parallel)$	-0.11(3)		-0.30(20)	-0.53(15)
$\mathbf{a}_0^2(\perp)$	0.23(7)		-1.20(1.00)	0.42(16)
$\text{Re}[\mathbf{a}_1^2(\parallel, \perp)]$	0.24(5)		0.80(20)	0.12(6)
$\mathbf{a}_2^2(\perp)$	-0.12(2)		-0.10(5)	-0.05(4)
$\mathbf{a}_0^4(\parallel)$	-0.03(1)		0.01(2)	
$\mathbf{a}_0^4(\perp)$	0.02(1)		0.25(23)	
$\text{Re}[\mathbf{a}_1^4(\parallel, \perp)]$	0.00(2)		0.05(6)	
$\mathbf{a}_2^4(\perp)$	-0.01(3)		0.10(8)	
Fast				
β	-0.02(2)	0.30(10)	0.20(10)	0.30(-)
$\text{Im}[\mathbf{a}_1^1(\parallel, \perp)]$	-0.05(1)	0.20(5)	0.23(5)	0.08(2)
$\mathbf{a}_0^2(\parallel)$	-0.22(6)		-0.40(20)	-0.62(20)
$\mathbf{a}_0^2(\perp)$	-0.32(10)		-0.60(20)	-0.06(4)
$\text{Re}[\mathbf{a}_1^2(\parallel, \perp)]$	0.11(2)		-0.10(15)	-0.31(6)
$\mathbf{a}_2^2(\perp)$	-0.07(1)		-0.03(1)	-0.11(4)
$\mathbf{a}_0^4(\parallel)$	-0.03(1)		-0.07(1)	0.03(3)
$\mathbf{a}_0^4(\perp)$	-0.10(2)		-0.05(1)	-0.19(3)
$\text{Re}[\mathbf{a}_1^4(\parallel, \perp)]$	-0.04(1)		-0.08(4)	-0.04(1)
$\mathbf{a}_2^4(\perp)$	0.03(2)		0.03(2)	0.15(4)

^aReferences 15 and 22.

^bReferences 21 and 25.

^cReference 26.

The molecular frame polarization parameters, expressed in the notation of Rakitzis and Zare,⁴¹ are presented in Table III, where they are compared with previously reported values.^{4,19,21–23,25,26} For the fast fragments, the polarization parameters that arise from incoherent excitation, $\mathbf{a}_0^2(\parallel)$ and $\mathbf{a}_0^2(\perp)$, which determine the M_J populations discussed above, are quite insensitive to photolysis wavelength. The coherent term $\mathbf{a}_2^2(\perp)$ is also roughly constant with photolysis wavelength, although it is somewhat reduced in magnitude at 223 nm compared to 248 and 193 nm. Substantial differences are seen between the three data sets for the $\text{Re}[\mathbf{a}_1^2(\parallel, \perp)]$ parameter, with the value reported here at 248 nm being of opposite sign to those obtained elsewhere in the first absorption band. In the diatomic limit, this parameter can be interpreted as arising from coherence between two states accessed via a parallel and a perpendicular transition and is related to the out-of-plane orientation term $\text{Im}[\mathbf{a}_1^1(\parallel, \perp)]$ by a simple phase factor.²¹ Thus, it is perhaps not surprising to find that $\text{Re}[\mathbf{a}_1^2(\parallel, \perp)]$ and $\text{Im}[\mathbf{a}_1^1(\parallel, \perp)]$

vary with dissociation wavelength in a similar fashion. Of course, the origin of these terms in the polyatomic case could reflect both static and dynamic coherence effects, as discussed further in Sec. III E.

Less obvious trends are observed for the slow products, which, we recall, are those most likely to be subject to the effects of non-axial recoil. The reported parameters are very similar to those measured by Lee *et al.* at 193 nm,²⁶ particularly in the case of the $\text{Im}[\mathbf{a}_1^1(\parallel, \perp)]$ parameter discussed further in Sec. III E. Although reasonable overall agreement is seen with the data by Rakitzis *et al.*,²⁵ large differences are found for the $\mathbf{a}_2^2(\perp)$ and $\text{Re}[\mathbf{a}_1^2(\parallel, \perp)]$ parameters, which were reported as being near limiting at 223 nm.²⁵ In the diatomic limit, the former parameter would indicate a substantial contribution to alignment arising from a perpendicular transition. The near-limiting value of $\text{Re}[\mathbf{a}_1^2(\parallel, \perp)]$ observed by Rakitzis *et al.*²⁵ at low velocities exhibited the opposite speed dependence to the $\text{Im}[\mathbf{a}_1^1(\parallel, \perp)]$ parameter measured by Kim *et al.*²¹ and Rakitzis *et al.*²² (see Sec. III E). The differences between $\text{Re}[\mathbf{a}_1^2(\parallel, \perp)]$ and $\text{Im}[\mathbf{a}_1^1(\parallel, \perp)]$ were taken to indicate different asymptotic phase differences for products emerging on the ground and excited state surfaces.²⁵ This would imply that dissociation via the $2^1A'$ and $1^1A''$ states contributes in similar ratios to pathways leading to both slow and fast products, somewhat at odds with previously reported values of $\beta(v)$ at 223 nm and with the discussion in Sec. III C. The authors also reported a series of $K=4$ parameters that appear to mirror the magnitude and speed dependence of their $K=2$ counterparts, which might suggest that for the slow fragments these parameters were not independently determined with the experimental geometries employed.²⁵

1. The long-range interaction model

In order to gain further insight into the dissociation mechanism and to help provide information about the pathways accessed in the long-range region, we apply a model developed previously to account for the orbital polarization in a number of systems.^{28,29,51,56} As reviewed in detail elsewhere,²⁷ the model predicts the Jacobi angle (γ) dependence of the PESs in the long-range region and of the atomic photofragment state multipoles that arise from their population, based on knowledge of the electrostatic interactions between atomic and molecular fragments. The potentials are evaluated at some arbitrarily defined critical distance R_c in the long-range region beyond which the atomic and molecular fragments lose contact. A number of assumptions apply to this model, principally that the electrostatic potential dominates other interactions, such as the dispersion interaction, and that the coherent population of multiple electronic states is ignored.

The $\text{CO}(X^1\Sigma^+)$ molecule possesses both a dipole ($-6.6 \times 10^{-40}\text{C m}$) and a quadrupole ($-3.7 \times 10^{-31}\text{C m}^2$) moment.^{57,58} Because $S(^1D_2)$ only possesses a quadrupole moment ($9.9 \times 10^{-40}\text{C m}^2$),⁵⁹ two types of interactions are used to describe the potential for $\text{CO}(X^1\Sigma^+) + S(^1D_2)$ at long range: the dipole-quadrupole and the quadrupole-quadrupole interaction. When evaluated at a large atom-molecule separation of 5 Å, these terms have the values of -3.9 and

-7.0 cm^{-1} , respectively. The R dependence of the two interaction terms means that the dipole-quadrupole interaction must dominate at sufficiently large separations. However, the quadrupole-quadrupole term is sufficiently large that it might dominate out to quite large values of R , and, therefore, the diagonalization of the long-range interaction matrix was carried out for both cases. The resultant potentials, and the $\rho_{KQ}(\gamma)$ predicted from them, are displayed in Fig. 10. The quadrupole-quadrupole potentials are identical in form to those calculated for $\text{O}(^1D_2) + \text{O}_2(^1\Delta_2)$ from the UV dissociation of ozone,²⁸ apart from the absence of the Λ doubling in the $\text{CO}(^1\Sigma^+)$ cofragment. State assignments have been made so that at linearity ($\gamma=0$), the lowest state is of Σ^+ symmetry. Although *ab initio* calculations are not available for this system in the long-range region, the present assignment is consistent with that of the quadrupole-quadrupole surfaces for $\text{O}(^1D_2) + \text{O}_2(^1\Delta_2)$, where the sign of the interaction is the same as that here, and with the *ab initio* work of Suzuki *et al.*⁴ shown in Fig. 1.

The Jacobi angle dependence of the state multipoles for dissociation on each of the long-range potentials is also shown in Fig. 10. At linearity ($\gamma=0^\circ$ for linear OCS), only the $\rho_{20}(\gamma)$ moment corresponding to the Δ state is positive, indicating a preferential alignment of $\mathbf{J} \parallel z$, consistent with the state yielding population only in $M_J = \pm 2$. (Note that in the calculations the molecular frame z axis lies along \mathbf{R} . At large R this becomes equivalent to the direction of recoil \mathbf{v} , which is defined as the z axis for the experimental molecular frame moments.²⁹) The other three states, characterized by $M_J = 1(\Pi)$ and $M_J = 0(\Sigma)$, exhibit a preference for $\mathbf{J} \perp z$, and thus a negative $\rho_{20}(\gamma)$, as expected. The behavior of the multipole moments away from linearity is complicated by the mixing of states of the same symmetry. This is most evident in the case of the quadrupole-quadrupole potentials. The lowest and highest energy A' surfaces can be seen to interact (most strongly at $\gamma=90^\circ$) as well as the two A'' surfaces. The pure orbital character of the surfaces is lost, i.e., M_J is not a valid quantum number, and this manifests itself in nonzero values for the mixing term $\rho_{21}(\gamma)$. Note that the S-atom orbitals of the $2^1A'(\Pi)$ state are symmetric with respect to bending motion in the plane of the molecule, while for the $1^1A'$ and $3^1A'(\Sigma^+/\Delta)$ surfaces the orbitals are aligned such that this symmetry is broken. Thus, the in-plane orbital occupancy of the $2^1A'(\Pi)$ state is independent of bending. As a result, the $2^1A'$ surface does not mix with the other A' surfaces, and the orbital character is conserved as γ is varied. This explains the angle independent $\rho_{20}(\gamma)$ and $\rho_{22}(\gamma)$ multipoles observed for this electronic state, and the fact that the $\rho_{21}(\gamma)$ multipole is zero at all values of γ . The behavior of the higher rank, $K=4$, multipoles is more complex and does not lend itself to such a simple interpretation.

2. Mechanistic interpretation

Experimental $\rho_{KQ}^{\text{mol}}(\theta)$ state multipoles calculated from the laboratory frame anisotropy parameters are displayed in Fig. 11. The experimental state multipoles for the fast fragments are characterized by the alignment of $\mathbf{J} \perp z$, as indicated by the negative values for $\rho_{20}^{\text{mol}}(\theta)$ and $\rho_{40}^{\text{mol}}(\theta)$ at all

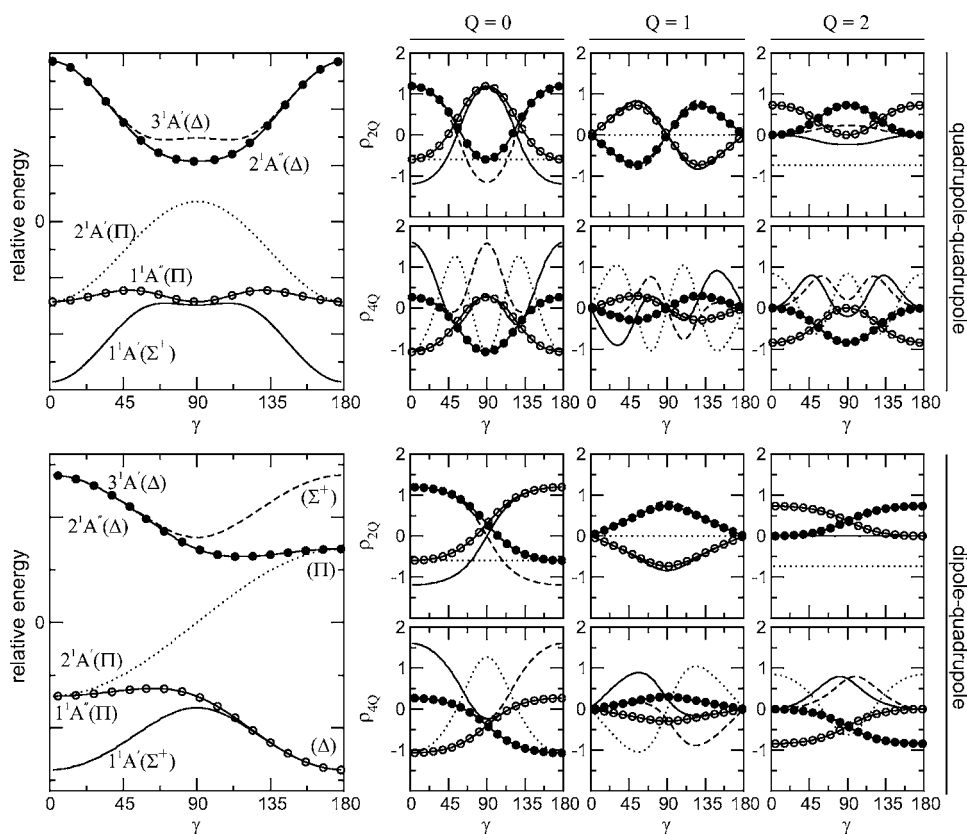


FIG. 10. Predicted long-range potentials and state multipoles for $S(^1D) + CO(X^1\Sigma)$ arising from the quadrupole-quadrupole and dipole-quadrupole interactions calculated as outlined in Sec. III D 1. Refer to the text for details of the electronic state assignments.

scattering angles. Interestingly, $\rho_{40}^{\text{mol}}(\theta)$ is significantly bigger than $\rho_{20}^{\text{mol}}(\theta)$. Small, but nonzero values of $\rho_{22}^{\text{mol}}(\theta)$ and $\rho_{42}^{\text{mol}}(\theta)$ are also observed, with a sign change associated with the change in rank. $\rho_{21}^{\text{mol}}(\theta)$ and $\rho_{41}^{\text{mol}}(\theta)$ are also of opposite sign (the absolute sign predicted for these parameters by the long-range model is difficult to determine, since it would require undertaking a full scattering calculation). A proposed mechanism should be able to account for all these patterns.

Conversion from the scattering angle θ to the Jacobi coordinate γ requires full account to be made of the scattering

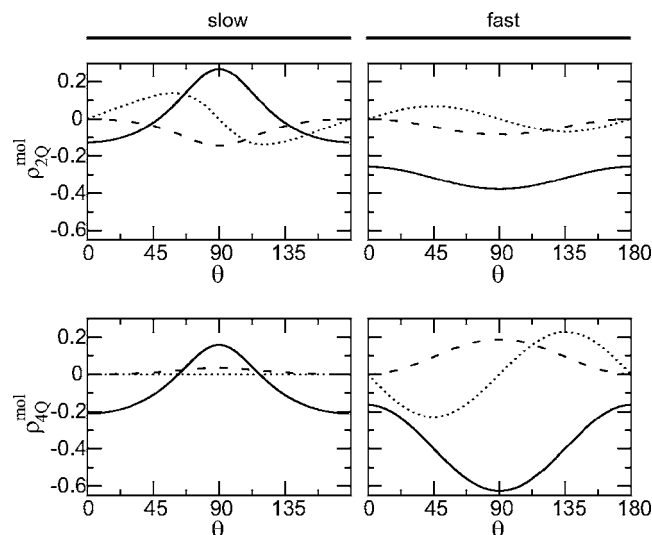


FIG. 11. Experimental J -state multipoles for slow and fast $S(^1D_2)$ products (see discussion for details). $Q=0$ (—), $Q=1$ (···), and $Q=2$ (---). An upper estimate of the errors associated with these results, propagated from the measured polarization parameters, is approximately 20%.

dynamics, and care must therefore be taken when comparing the experimental $\rho_{KQ}^{\text{mol}}(\theta)$ with the calculated $\rho_{KQ}(\gamma)$ presented above. For this reason the present discussion of the polarization parameters is necessarily qualitative in nature. Nevertheless, a crude measure of the range of Jacobi angles accessed during dissociation can be gained by comparing the classical rotational period, τ , for $CO(X^1\Sigma^+)$, which is assumed to be a free rotor, with the time taken by the system to reach the critical distance (here taken to be 5 Å). For fast fragments partnered by CO molecules with $J_{CO} \sim 26$, $\tau_f \sim 3.5 \times 10^{-13}$ s, while for slow fragments, where $J_{CO} \sim 49$, $\tau_s \sim 2 \times 10^{-13}$ s. Assuming that the relative velocity of the fragments is constant, rough estimates of the separation times for these two cases are $t_f = 9 \times 10^{-14}$ s and $t_s = 2 \times 10^{-13}$ s. In the former case, the period of rotation is considerably longer than the time of arrival at R_c , indicating that small γ angles should be preferentially accessed, while for the slow fragments, the sampling of γ will be more uniform. Note that these conclusions reinforce the view that interpretation of the polarization of the slow (high J_{CO}) fragments will be significantly harder than for the fast photofragments. Given the above estimates of the time scales involved in the dissociation of OCS, it is also worth attempting to quantify the effects of any vibrational angular momentum on the dissociation mechanism, as mentioned briefly in Sec. III C. It is readily established that rotation of the plane of the excited OCS molecule about the original OCS axis, due to excitation of nonzero values of the vibrational angular momentum, $l \sim 1$, leads to very small deflection angles ($\leq 2^\circ$) on the dissociation time scales mentioned above.

Comparison of the experimental and theoretical state multipoles for both dipole-quadrupole and quadrupole-

quadrupole interactions suggests that either of the three lowest singlet surfaces generate the required negative values of $\rho_{20}(\gamma)$ and $\rho_{40}(\gamma)$ in the region around $\gamma=0^\circ$. However, for the quadrupole-quadrupole interaction only the $1^1A'$ and $2^1A'$ surfaces also give rise to a negative $\rho_{22}(\gamma)$ and a positive $\rho_{42}(\gamma)$, as seen in the experiments. When dipole-quadrupole interactions are considered, only the $2^1A'(\text{II})$ surface matches the experimental moments with $Q=0$ and 2. Although the experimental and predicted multipoles cannot be quantitatively compared, the polarization data are consistent with the $2^1A'$ surface playing the dominant role in the exit channel leading to fast S(1D_2) products.

Products emerging exclusively on the $2^1A'$ state are predicted to possess zero values of $\rho_{21}(\gamma)$ within the long-range model, contrary to what is observed experimentally. In fact, the $2^1A'$ surface is the only one of the five PESs shown in Fig. 11 that leads to zero values of $\rho_{21}(\gamma)$. A small contribution from excitation to, and dissociation on, the $1^1A'$ ($1^1\Sigma^-$) surface might provide one explanation for the nonzero values of $\rho_{21}(\gamma)$ for the fast products, and its participation in the dynamics would also be expected to affect the values observed for the other $\rho_{KQ}^{\text{mol}}(\theta)$ moments. In many cases the $\rho_{KQ}(\gamma)$ arising from dissociation on the $1^1A''$ surface have opposite signs to those predicted for dissociation on the $2^1A'$ surface, and this may explain why the experimental $\rho_{KQ}^{\text{mol}}(\theta)$ moments, even at their peak values, are smaller than predicted for the $2^1A'$ surface by the long-range model. Note that the magnitudes of the moments might also be reduced from their limiting values by rotation of the forming CO cofragment, but this mechanism is not predicted by the long-range model to play a role for the $K=2$ moments from the $2^1A'$ surface, since these are found to be independent of Jacobi angle, γ . If the $1^1A''$ were included as a small 10% weighted incoherent contribution to the modeled dynamics, a better match between theory and experiment might be achieved, and the nonzero value of $\rho_{21}(\theta)$ explained. However, as discussed further in Sec. III E in the context of the orientation parameters, two other effects may also account for the origin of the nonzero $\rho_{21}(\theta)$ moment, namely, the dynamic coherence arising from simultaneous excitation of the $2^1A'$ and $1^1A''$ states and/or the static coherence subsequent to excitation to the $2^1A'$ state alone.

A similar approach can be used to help identify the asymptotic surfaces populated in the production of the slow fragments. The experimental state multipoles that characterize the polarization of the slow fragments are also shown in Fig. 11. The scattering angle averaged ρ_{KQ}^{mol} moments for the slow fragments indicate that ρ_{20}^{mol} and ρ_{42}^{mol} are positive, while ρ_{22}^{mol} and ρ_{40}^{mol} are both negative. Considering the quadrupole-quadrupole interaction alone, population of the $1^1A'$ surface provides the best model for the experimental ρ_{KQ}^{mol} moments, since only this surface generates products with positive ρ_{20}^{mol} and negative ρ_{22}^{mol} moments. This interpretation is in accordance with the 2D wave packet calculations of Suzuki *et al.*⁴ However, the signs of the predicted $\rho_{KQ}(\gamma)$ moments for $Q=0$ and 2 are different if the dipole-quadrupole interaction is considered to dominate at R_c . Unlike dissociation on the $2^1A'$ surface leading to fast photofragments, dissociation proceeding via nonadiabatic transfer to the ground $1^1A'$

state would, within the long-range model, lead to a nonzero ρ_{21}^{mol} moment, as observed experimentally for the slow fragments. As with the fast fragments, the present model leaves some room for a small contribution from the $1^1A''$ surface in the dynamics leading to production of the slow products. However, given that nonaxial recoil plays such a significant role in the dissociation of these fragments, it seems premature to speculate further in the absence of a rigorous theory to account for polarization effects in polyatomic systems.

E. Orbital orientation

As shown in Fig. 8 and Table II, nonzero values for all of the $K=1$ and 3 rank orientation parameters were observed. In the diatomic limit, these have specific mechanistic implications: α_1 arises from the excitation of a perpendicular transition, while γ_1 and γ'_1 are the manifestation of interference effects between coherently excited states accessed via a parallel and a perpendicular transition. The interpretation in the case of triatomic systems is not so straightforward. For example, as noted in the preceding section concerning the even K , $Q=1$ moments, γ'_1 (proportional to $\text{Im}[\mathbf{a}_1^1(\parallel, \perp)]$) can arise as a consequence of static or dynamic coherence, in addition to the long-range effects discussed above, and distinguishing these various mechanisms can be difficult.

The velocity-averaged values of $\text{Im}[\mathbf{a}_1^1(\parallel, \perp)]$ are presented in Table III, where they are compared with the results from previous studies. Kim *et al.* used the REMPI TOF core-extracted technique to measure $\text{Im}[\mathbf{a}_1^1(\parallel, \perp)]$ following dissociation at 223 nm.²¹ This was found to be near zero at low velocity, steadily increasing to a maximum value of $\text{Im}[\mathbf{a}_1^1(\parallel, \perp)]=0.25$. Kim *et al.* interpreted the speed dependence of $\text{Im}[\mathbf{a}_1^1(\parallel, \perp)]$ as arising from a dynamic coherence phenomenon.²¹ They used the velocity dependence of β to estimate the relative contributions from the $2^1A'$ and $1^1A''$ states at a given speed, which they then used to model satisfactorily the speed dependence of the orientation parameter. More recently, Rakitzis *et al.* have measured the orbital orientation following dissociation at 230 nm:²² although only a speed averaged value for the fast component was reported, this was found to be in agreement with the work of Kim *et al.* $\text{Im}[\mathbf{a}_1^1(\parallel, \perp)]$ has also been measured by Van den Brom *et al.*,²³ who were able to determine its speed dependence as a function of parent molecule vibrational level. The speed variation was found to be similar to that seen by Kim *et al.*,²¹ particularly when the data were averaged over the parent vibration. The v_2 resolved measurements were taken to indicate that excitation to the $2^1A'$ state plays a larger role for parent molecules with one quantum in the bending vibration. The value of the $\text{Im}[\mathbf{a}_1^1(\parallel, \perp)]$ parameter obtained in the present study, though much smaller than those reported Kim *et al.*,²¹ Rakitzis *et al.*,²² and Van den Brom *et al.*,²³ has a similar speed dependence to that found previously²¹ at other wavelengths. The velocity-averaged values of $\text{Im}[\mathbf{a}_1^1(\parallel, \perp)]$ obtained here at 248 nm are similar in magnitude to those observed by Lee *et al.* at 193 nm.²⁶

In the light of the discussion of the translational anisotropy, and the rather minor role inferred for the $1^1A''$ state, it seems most likely that the $\text{Im}[\mathbf{a}_1^1(\parallel, \perp)]$ values observed

here, and elsewhere in this absorption band, primarily reflect static coherence effects arising from excitation of the $2^1A'$ surface alone. In the past, the possibility of static coherence arising from excitation to the $2^1A'$ surface was discounted on the basis of the small perpendicular projection of the transition dipole moment on the recoil axis.^{21–23} However, the results of the simulations presented in Sec. III C suggest that the transition moment for excitation into the $2^1A'$ state may have significant parallel and “perpendicular” components, with respect to both the initial direction of the C–S bond and the final recoil direction. The variation observed in $\text{Im}[a_1(\parallel, \perp)]$ with recoil velocity^{21–23,26} might then arise from the different parallel and perpendicular components of the transition moment for the $2^1A'$ state relative to the recoil direction of the S atom. The variations in these components might be expected to mirror the variations in β with velocity, as noted previously.^{21,26}

In the case of photodissociation of a triatomic molecule, the generation of in-plane orientation of the atomic angular momentum, as characterized by α_1 and γ_1 , is largely an unexplored area. Only a handful of measurements of the relevant parameters have been reported to date.^{26,28,42,60,61} With one exception,²⁸ these studies returned zero^{42,60} or small²⁶ values for the in-plane orientation moments. In the present case, the reported parameters are substantially larger than those observed in previous studies (including our own work on the first nonzero measurements of $K=1$ parameters in ozone²⁸). Suits and co-workers have explained the observed zero or near-zero values in terms of conservation of the helicity imparted by the dissociating photon.^{26,42} The helicity quantum number Ω is not a valid quantum number for a single state of a bent triatomic molecule, and thus the photon helicity is quenched in the dissociation process. It has been argued in the case of ozone that coherent excitation of two surfaces may relax this constraint and allow in-plane orientation to be imparted on the atomic fragments.²⁸ It is possible that a similar phenomenon is responsible for the present findings. Whatever the interpretation, the current measurements reveal that α_K and γ_K for $K=1$ and 3 can all be nonzero in the case of a bent triatomic molecule.

F. Comparison with N₂O

It is interesting to compare the present system with the isovalent molecule N₂O. The main transition responsible for UV photoabsorption in N₂O is the electronically forbidden, vibronically allowed, $2^1A'(\Delta) \leftarrow 1^1A'(^1\Sigma^+)$ transition, as in the case of OCS. As a result, the absorption spectra of the two molecules are very similar⁶² and exhibit a similar dependence on temperature.⁶³ The surfaces accessible are also similar to those of OCS displayed in Fig. 1. The dynamics leading to the O(¹D₂) product has been investigated by a number of groups^{44,51–54,64–68} in the region of maximum absorption cross section around 180 nm. As is the case for OCS, little energy is deposited into vibration of the N₂ molecular fragment,^{53,64–67} which has been rationalized in terms of the similar N₂ bond lengths as the free molecule and in N₂O.⁴⁸ As was shown in Fig. 5, the β parameters reported for the singlet products are positive but considerably smaller

than their limiting value expected after excitation into the $2^1A'$ state.^{52,53,64,66–68} This has been taken to indicate that, as is the case in OCS, the system undergoes bending prior to dissociation in this wavelength region,^{48,49,53,55} consistent with the modeling shown in Fig. 5. In the recent high resolution study of Kawamata *et al.* at $\lambda \sim 204$ nm,⁵² β parameters were determined for a range of J_{N_2} rotational states (these data are also reproduced in the bottom panel of Fig. 5). As with previous work on OCS,⁴ the variation in β with J_{N_2} was in this case interpreted in terms of varying contributions to absorption and dissociation from the $2^1A'$ and $1^1A''$ surfaces. However, in the light of the modeling shown in Fig. 5, and current theory,^{48,49,53,55} it seems more likely that excitation to the $2^1A'$ state dominates, and the trends in β with J_{N_2} largely reflect the effects of nonaxial recoil.

Angular momentum alignment has been measured by Chandler and co-workers^{53,54} and by Ahmed *et al.*,⁶⁸ most recently including all contributions up to $K=4$.⁴⁴ Suzuki *et al.* have interpreted the recovered M_J populations in terms of a long-range model similar to the one described here and concluded that the dominant dissociation channel is via adiabatic dissociation on the $2^1A'$, the same as the mechanism proposed for OCS dissociation.⁴ In their most recent work Smolin *et al.* report a large value for the coherent term γ_2 ,⁴⁴ which was interpreted to indicate the possibility of some participation of the $2^1A''$ surface to the dynamics, but such a large role for this state is not consistent with theory.^{48,49} However, contrary to OCS, the dissociation in N₂O has generally been described in terms of adiabatic processes^{44,53,54} with no indication of a product pathway involving internal conversion to the ground state, as has been observed in the case for OCS. The implications of this for the triplet dissociation channel in N₂O are discussed further in the subsequent paper.⁵

IV. CONCLUSIONS

The speed distribution, translational anisotropy, and angular momentum polarization of the S(¹D₂) atomic photo-fragments have been determined subsequent to photodissociation of OCS in the red wing of the first absorption band at 248 nm. The speed distribution is similar to those measured previously at this and other wavelengths. Two product speed regimes have been identified, consistent with the nonadiabatic dissociation involving the $2^1A'$ and $1^1A'$ PESs predicted by the 2D quantum dynamical calculations of Suzuki *et al.*⁴ Although the translational anisotropy data are also in good agreement with previous work, it is shown here that its speed dependence can be modeled as arising from nonaxial recoil subsequent to absorption predominantly to the $2^1A'$ electronic state. The simulations indicate that excitation to the $1^1A''$ state may play a rather minor role, consistent with the quantum dynamical calculations of Suzuki *et al.*⁴ Although the interpretation of the atomic angular momentum polarization is complicated by the effects of nonaxial recoil, these are shown to be relatively minor for the fast fragments. Using the predictions of a previously discussed long-range model, the polarization parameters obtained for these fragments are shown to be consistent with the predominant ex-

citation to, and dissociation on, the $2^1A'$ state. Relatively large nonzero in-plane and out-of-plane orientation parameters have also been observed. Unlike previous work, and in the light of the modeling of the translational anisotropy, the latter is ascribed to static coherence arising from excitation principally to the $2^1A'$ state.

ACKNOWLEDGMENTS

We gratefully acknowledge the EPSRC for research grants. We also gratefully acknowledge helpful discussions with Professor O. S. Vasyutinskii (Ioffe Institute, St. Petersburg) and Professor Gerrit C. Groenenboom (Radboud University, Nijmegen).

- ¹R. P. Wayne, *Chemistry of Atmospheres*, 3rd ed. (Oxford University Press, Oxford, 2000).
- ²IUPAC Subcommittee on Gas Kinetic Data Evaluation—Data Sheet PSOx1, http://www.iupac-kinetic.ch.cam.ac.uk/datasheets/photol/PSOx1OCS_hv.pdf (2001).
- ³C. E. Strauss, G. C. McBane, P. L. Houston, I. Burak, and J. W. Hepburn, *J. Chem. Phys.* **90**, 5364 (1989).
- ⁴T. Suzuki, H. Katayanagi, S. Nanbu, and M. Aoyagi, *J. Chem. Phys.* **109**, 5778 (1998).
- ⁵M. Brouard, F. Quadrini, and C. Vallance, *J. Chem. Phys.* **127**, 074305 (2007).
- ⁶J. W. Rabalais, J. M. McDonald, V. Scherr, and S. P. McGlynn, *Chem. Rev. (Washington, D.C.)* **71**, 73 (1971).
- ⁷W. H. Breckenridge and H. Taube, *J. Chem. Phys.* **52**, 1713 (1970).
- ⁸M. I. McCarthy and V. Vaida, *J. Phys. Chem.* **92**, 5875 (1988).
- ⁹C. Cossart-Magos, M. Jungen, R. Xu, and F. Launay, *J. Chem. Phys.* **119**, 3219 (2003).
- ¹⁰N. Sivakumar, I. Burak, W. Y. Cheung, P. L. Houston, and J. W. Hepburn, *J. Phys. Chem.* **89**, 3609 (1985).
- ¹¹N. Sivakumar, G. E. Hall, P. L. Houston, J. W. Hepburn, and I. Burak, *J. Chem. Phys.* **88**, 3692 (1988).
- ¹²Y. Sato, Y. Matsumi, M. Kawasaki, K. Tsukiyama, and R. Bersohn, *J. Phys. Chem.* **99**, 16307 (1995).
- ¹³A. Sugita, M. Mashino, M. Kawasaki, Y. Matsumi, R. Bersohn, G. Trotter-Kriegeskort, and K. H. Gericke, *J. Chem. Phys.* **109**, 5778 (1998).
- ¹⁴H. Katayanagi and T. Suzuki, *Chem. Phys. Lett.* **360**, 104 (2002).
- ¹⁵A. J. van den Brom, T. P. Rakitzis, J. van Heyst, T. N. Kitsopolous, S. R. Jezowski, and M. H. M. Janssen, *J. Chem. Phys.* **117**, 4255 (2002).
- ¹⁶T. P. Rakitzis, A. J. van den Brom, and M. H. M. Janssen, *Science* **303**, 1852 (2004).
- ¹⁷A. J. van den Brom, T. P. Rakitzis, and M. H. M. Janssen, *J. Chem. Phys.* **121**, 11645 (2004).
- ¹⁸M. L. Lipciuc and M. H. M. Janssen, *Phys. Chem. Chem. Phys.* **8**, 3007 (2006).
- ¹⁹Y. Mo, H. Katayanagi, M. C. Heaven, and T. Suzuki, *Phys. Rev. Lett.* **77**, 830 (1996).
- ²⁰H. Katayanagi, Y. Mo, and T. Suzuki, *Chem. Phys. Lett.* **247**, 571 (1995).
- ²¹Z. H. Kim, A. J. Alexander, and R. N. Zare, *J. Phys. Chem. A* **103**, 10144 (1999).
- ²²T. P. Rakitzis, P. C. Samartzis, and T. N. Kitsopolous, *J. Chem. Phys.* **111**, 10415 (1999).
- ²³A. J. van den Brom, T. P. Rakitzis, and M. H. M. Janssen, *J. Chem. Phys.* **123**, 164313 (2005).
- ²⁴M. H. Kim, W. Li, S. K. Lee, and A. G. Suits, *Can. J. Chem.* **82**, 880 (2004).
- ²⁵T. P. Rakitzis, P. C. Samartzis, and T. N. Kitsopolous, *Phys. Rev. Lett.* **87**, 123001 (2001).
- ²⁶S. K. Lee, R. Silva, S. Tahamanna, O. S. Vasyutinskii, and A. G. Suits, *J. Chem. Phys.* **125**, 144318 (2006).
- ²⁷A. P. Clark, R. Cireasa, M. Brouard, F. Quadrini, and C. Vallance, in *Molecular Reaction and Photodissociation Dynamics in the Gas Phase*, edited by P. D. Kleiber and K. C. Lin (Research Signpost, India, 2007).
- ²⁸M. Brouard, R. Cireasa, A. P. Clark, G. C. Groenenboom, G. Hancock, S. J. Horrocks, F. Quadrini, G. A. D. Ritchie, and C. Vallance, *J. Chem. Phys.* **125**, 133308 (2006).
- ²⁹M. Brouard, R. Cireasa, A. P. Clark, T. J. Preston, C. Vallance, G. C. Groenenboom, and O. S. Vasyutinskii, *J. Phys. Chem. A* **108**, 7965 (2004).
- ³⁰A. T. J. B. Eppink and D. H. Parker, *Rev. Sci. Instrum.* **68**, 3477 (1997).
- ³¹D. W. Chandler and P. L. Houston, *J. Chem. Phys.* **87**, 1445 (1987).
- ³²M. Bass, M. Brouard, A. P. Clark, and C. Vallance, *J. Chem. Phys.* **117**, 8723 (2002).
- ³³M. J. Bass, M. Brouard, A. P. Clark, B. Martínez-Haya, and C. Vallance, *Phys. Chem. Chem. Phys.* **5**, 856 (2003).
- ³⁴M. Brouard, A. P. Clark, C. Vallance, and O. S. Vasyutinskii, *J. Chem. Phys.* **119**, 771 (2003).
- ³⁵B. Martínez-Haya, M. J. Bass, M. Brouard, C. Vallance, I. Torres, and J. Barr, *J. Chem. Phys.* **120**, 11042 (2004).
- ³⁶M. Brouard, R. Cireasa, A. P. Clark, F. Quadrini, and C. Vallance, *Phys. Chem. Chem. Phys.* **8**, 5549 (2006).
- ³⁷NIST Atomic Spectra Database, <http://physics.nist.gov/PhysRefData/ASD/index.html> (Version 3, 2005).
- ³⁸B. Y. Chang, R. C. Hoetzlein, J. A. Mueller, J. D. Geiser, and P. L. Houston, *Rev. Sci. Instrum.* **69**, 1665 (1998).
- ³⁹A. S. Bracker, E. R. Wouters, A. G. Suits, and O. S. Vasyutinskii, *J. Chem. Phys.* **110**, 6749 (1999).
- ⁴⁰L. D. A. Siebbeles, M. Glass-Maujean, O. S. Vasyutinskii, J. A. Beswick, and O. Roncero, *J. Chem. Phys.* **100**, 3610 (1994).
- ⁴¹T. P. Rakitzis and R. N. Zare, *J. Chem. Phys.* **110**, 3341 (1999).
- ⁴²S. K. Lee, D. Townsend, O. S. Vasyutinskii, and A. G. Suits, *Phys. Chem. Chem. Phys.* **7**, 1650 (2005).
- ⁴³B. V. Pichayev, A. G. Smolin, and O. S. Vasyutinskii, *J. Phys. Chem.* **101**, 7614 (1997).
- ⁴⁴A. G. Smolin, O. S. Vasyutinskii, E. R. Wouters, and A. G. Suits, *J. Chem. Phys.* **121**, 6759 (2004).
- ⁴⁵A. P. Clark, M. Brouard, F. Quadrini, and C. Vallance, *Phys. Chem. Chem. Phys.* **8**, 5591 (2006).
- ⁴⁶A. J. Alexander, *J. Chem. Phys.* **118**, 6234 (2003).
- ⁴⁷A. V. Demyanenko, V. Dribinski, H. Reisler, H. Meyer, and C. X. W. Quian, *J. Chem. Phys.* **111**, 7383 (1999).
- ⁴⁸A. Brown, P. Jimeno, and G. G. Balint-Kurti, *J. Phys. Chem. A* **103**, 11089 (1999).
- ⁴⁹M. N. Daud, G. G. Balint-Kurti, and A. Brown, *J. Chem. Phys.* **122**, 054305 (2005).
- ⁵⁰T. P. Rakitzis, A. J. van den Brom, and M. H. M. Janssen, *Chem. Phys. Lett.* **372**, 187 (2003).
- ⁵¹J. M. Teule, G. C. Groenenboom, D. W. Neyer, D. W. Chandler, and M. H. M. Janssen, *Chem. Phys. Lett.* **320**, 177 (2000).
- ⁵²H. Kawamata, H. Kohguchi, T. Nishide, and T. Suzuki, *J. Chem. Phys.* **125**, 133312 (2006).
- ⁵³D. W. Neyer, A. J. R. Heck, and D. W. Chandler, *J. Chem. Phys.* **110**, 3411 (1999).
- ⁵⁴D. W. Neyer, A. J. R. Heck, D. W. Chandler, J. M. Teule, and M. H. M. Janssen, *J. Phys. Chem. A* **103**, 10388 (1999).
- ⁵⁵S. Nanbu and M. S. Johnson, *J. Phys. Chem. A* **108**, 8905 (2004).
- ⁵⁶A. M. Coroiu, D. H. Parker, G. C. Groenenboom, J. Barr, I. T. Novalbos, and B. J. Whitaker, *Eur. Phys. J. D* **38**, 151 (2006).
- ⁵⁷U. Buontempo, S. Cunsolo, and G. Jaccucci, *J. Chem. Phys.* **59**, 3750 (1973).
- ⁵⁸S. Coriani, A. Halkier, D. Jonsson, J. Gauss, A. Rizzo, and O. Christiansen, *J. Chem. Phys.* **118**, 7329 (2003).
- ⁵⁹K. Andersson and A. J. Sadlej, *Phys. Rev. A* **46**, 2356 (1992).
- ⁶⁰W. Denzer, S. J. Horrocks, P. J. Pearson, and G. A. D. Ritchie, *Phys. Chem. Chem. Phys.* **8**, 1954 (2006).
- ⁶¹S. J. Horrocks, P. J. Pearson, and G. A. D. Ritchie, *J. Chem. Phys.* **125**, 133313 (2006).
- ⁶²K. Yoshino, D. E. Freeman, and W. H. Parkinson, *Planet. Space Sci.* **32**, 1219 (1982).
- ⁶³G. S. Selwyn and H. S. Johnston, *J. Chem. Phys.* **74**, 3791 (1981).
- ⁶⁴P. Felder, B. M. Haas, and J. R. Huber, *Chem. Phys. Lett.* **186**, 177 (1991).
- ⁶⁵T. F. Hanisco and A. C. Kummel, *J. Phys. Chem.* **97**, 7242 (1993).
- ⁶⁶L. L. Springsteen, S. Satyapal, Y. Matsumi, M. Dobeck, and P. L. Houston, *J. Phys. Chem.* **97**, 7239 (1993).
- ⁶⁷T. Suzuki, H. Katayanagi, Y. Mo, and K. Tonokura, *Chem. Phys. Lett.* **256**, 90 (1996).
- ⁶⁸M. Ahmed, E. R. Wouter, D. S. Peterka, O. S. Vasyutinskii, and A. G. Suits, *Faraday Discuss.* **113**, 425 (1999).
- ⁶⁹O. S. Vasyutinski (private communication).